

Bulk fracture anisotropy in Cold-Sprayed Al 6061 deposits

Scott E. Julien^{a,*}, Ahmad Nourian-Avval^a, Wentao Liang^b, Tricia Schwartz^b, Ozan C. Ozdemir^a, Sinan Müftü^a

^a Department of Mechanical and Industrial Engineering, Northeastern University, Boston, MA 02115, USA

^b Kostas Research Institute for Homeland Security, Northeastern University, Burlington, MA 01803, USA



ARTICLE INFO

Keywords:

Cold spray
Additive manufacturing
Fracture toughness
Anisotropy
Mechanical properties

ABSTRACT

Tensile and fracture anisotropy were studied in helium-sprayed bulk Al 6061 cold spray deposits. Tensile properties (elastic modulus, yield strength, tensile strength, and elongation at break) were measured in the two in-plane principal deposit directions (long-rastering, and stepping), and fracture toughness was characterized for six principal load/crack direction pairs defined with respect to the spray directions. No in-plane anisotropy was measured for the tensile properties, attributed to uniform in-plane microstructure. Fracture toughness was found to be mildly transversely isotropic, with equal values when crack propagation was in-plane (mean of $11.0 \text{ MPa}\sqrt{\text{m}}$) and slightly higher values when crack propagation was out-of-plane (through the deposit thickness, mean of $13.0 \text{ MPa}\sqrt{\text{m}}$). The overall fracture toughness range was 40–50% that of wrought Al 6061-T6. In-plane fracture was almost completely interparticular (fracture along particle interfaces), while out-of-plane fracture was a mixture of interparticular and transparticular (fracture through particles). A greater amount of transparticular fracture was observed in orientations with higher toughness. Overall, the low level of anisotropy was attributed to good interparticle bonding as a result of effective spray parameters and the use of helium as the accelerating gas.

1. Introduction

Cold spray is a material deposition process whereby solid powder material is deposited onto a substrate at temperatures below the melting points of the materials. This is achieved by accelerating the powder particles (typically $5\text{--}50 \mu\text{m}$ in diameter) in a high velocity gas stream (typically helium, nitrogen, or air) through a converging-diverging de Laval nozzle [1]. The particles reach extremely high velocities (typically in the range of $300\text{--}1500 \text{ m/s}$) and, upon impact with the substrate, undergo significant plastic deformation. If a minimum critical velocity is reached – dependent upon such factors as powder and substrate material, particle size, and particle impact temperature – bonding with the substrate occurs. Typically, deposits are formed by repeatedly moving the nozzle across a substrate in a raster pattern. The nozzle is held at a fixed standoff distance and angle above the substrate; traversed in a line, depositing a single track; stepped transversely a prescribed distance; then traversed along a line parallel to the first. Repeating this pattern builds a single, two-dimensional, rectangular layer. Successively depositing layers over the same area allows a deposit to be built to a desired height. Robotic systems are often used to perform this task repeatably, so as to build the deposit in a controlled manner [2].

* Corresponding author at: Department of Mechanical and Industrial Engineering, Northeastern University, 360 Huntington Ave, SN 334, Boston, MA 02115, USA.

E-mail address: s.julien@northeastern.edu (S.E. Julien).

Cold spray technology is attractive in such applications as the repair of aluminum or magnesium aerospace components, where high-temperature processes (i.e. above the melting point of the materials) can cause unacceptable oxidative reactions, phase changes, or residual stress buildup during deposition [2]. The process is presently used for dimensional restoration of worn/damaged parts, applying thermal/wear-resistant coatings [3], and for additively manufacturing components that bear light loads [1]. However, there is increasing demand for the technology to be used in higher load-bearing applications. In order to realize this, the mechanical properties of deposits (e.g. tensile, fracture, and fatigue strengths) and their relationship to the process parameters must be understood.

Cold spray coatings typically exhibit compressive residual stresses [1], which impart resistance to fracture and fatigue cracking. However, because of the significant amount of cold working involved in the particle impact process, the coatings also typically possess high strength but low ductility [1]. Numerous studies have characterized the tensile properties (e.g. yield strength, tensile strength, and elongation) of cold spray coatings [4–7]. While tensile properties such as ultimate tensile strength and elongation to break can provide a measure of a material's ability to resist cohesive failure, fracture toughness is more applicable in situations where the material possesses stress-concentrating flaws. This is particularly the case for cold spray, where deposits possess a high density of intrinsic flaws in the form of unbonded regions between particles. Despite this, few studies have characterized the fracture properties – in particular, the critical fracture toughness – of cold spray deposits [5,8–11].

Many studies characterizing the ability of a cold spray material to resist interfacial or bulk fracture have characterized the adhesive (deposit-to-substrate) or cohesive “strength” of deposits. A number of studies [12–16] have utilized the ASTM C633 bond test [17], which gives results as a cohesive or adhesive “bond strength” of the deposit or interface, often in units of MPa or psi. While the method is easy to apply and useful for quick benchmarking, it is limited to cases where the deposit or interface strength is less than the strength of the epoxy (typically 70 MPa or less) [12]. A modified version that does not require the use of an epoxy has been utilized [12], as well as modified tensile tests [18,19], three-point bend tests [19], and a pin adhesion test [20]. A tubular coating tensile (TCT) test has been used [21] to test the in-plane cohesive strength of thin coatings, and shear methods such as the triple-lug shear test [22,23], the single-lug shear test [16,24,25], and a modified single-lug shear test [26] have been used to characterize the adhesive or cohesive strength in shear.

All of the above tests are generally straightforward to apply and give a reasonable estimate of the ability of the material to resist cohesive or adhesive failure. From a practical standpoint, they are suitable for most applications, such as comparative studies and quality benchmarking. From a fundamentals standpoint, however, the metrics they produce are not fundamental properties of the deposit or interface that are independent of test methodology. Furthermore, the location of failure onset and the direction of final crack propagation cannot be well-controlled, and fracture can sometimes initiate and propagate at several locations, simultaneously. Fracture mechanics methods, by contrast, employ an initial pre-crack and a loading configuration that allows the failure crack to propagate in a controlled manner. Furthermore, the critical fracture toughness that they produce is a fundamental interfacial or material property that is test-independent when sound testing methodology is used.

Several common fracture mechanics-based standards exist for measuring the fracture toughness of metals, in general. ASTM E399 [27] is used to measure the plane strain fracture toughness, K_{Ic} , of metals that fracture in a linear-elastic fashion (i.e. do not exhibit appreciable plastic deformation during testing). ASTM E561 [28] is used to measure the plane stress fracture resistance (K_R) curve for metals that exhibit an appreciable amount of plastic tearing. ASTM E1820 [29] is used to measure the plane strain fracture toughness, K_{Ic} , value or fracture resistance, K_R , curve of metals that exhibit either linear-elastic or elastic-plastic fracture. All of these methods specify standard specimen geometries, specimen preparation and testing procedures, data analysis methods, and result qualification criteria.

In the cold spray literature, several groups have studied the critical fracture toughness of deposits. Bakshi, et al. [8], employed the single-edge bend test in ASTM E399 to determine the through-thickness fracture toughness of helium-sprayed aluminum (Al) 1100 alloy on Al 1100 substrate. Bangstein, et al. [9] employed the ASTM E399 compact tension specimen geometry to study the bulk in-plane fracture toughness of nitrogen-sprayed Al 6061 deposits. White, et al. [10] conducted interfacial fracture testing of helium-sprayed Al 7075 on7075-T6, using the compact tension and four-point bend tests. Gavras et al. [5] used the ASTM E647 [30] compact tension specimen to characterize, among other properties, the maximum fatigue stress intensity factor (SIF) – analogous to the fracture toughness – for fatigue crack growth rate in bulk helium-sprayed Al 6061 coatings. Kovarik, et al. [11] used the ASTM E1820 single-edge bend test to characterize the through-thickness fracture toughness of nitrogen-sprayed pure Al coatings, among other metals.

Although all of these studies have contributed to an understanding of the ability of cold spray deposits to resist fracture under critical load, as cold spray gains more widespread use as an additive manufacturing technology – allowing the fabrication of complex parts with complex loading configurations are – an understanding of how cold sprayed material responds in all loading directions is necessary. Unlike bulk metals, however, which can often be treated as homogeneous and isotropic, cold spray deposits are micro-structurally anisotropic, consisting of severely deformed particles that are significantly flattened in the through-thickness direction [31–33]. Within particles, microstructure is also inhomogeneous, with inhomogeneous cold working indicated by fine grain structures at the particle boundaries [31,34,35]. Furthermore, particle-particle bonding is often non-uniform along particle interfaces [35–37]. As such, it is intuitive to expect the mechanical properties of cold spray deposits to be anisotropic.

To date, mechanical anisotropy in cold spray deposits has only been studied by several groups, for elastic modulus [31,38,39], hardness [31,32,34,39], and tensile properties (yield strength, tensile strength, and/or elongation at break) [31,32,34,40]. These studies have encompassed several commonly sprayed metals, including Cu [31,32,34,38], Ni [38], Al [38], Ti [38], and Ta [39], with Cu being the most commonly studied, thus far. The studies have also encompassed a variety of spray parameters, including the three most common spray gases: air [34], nitrogen [32,39], and helium [31,40]. Some studies have found measured properties to be anisotropic in the coatings studied [31,32,34], while others have found them to be isotropic [38–40]. In one study, elastic modulus was

characterized by resonant ultrasound spectroscopy (RUS) and was found to be nearly perfectly isotropic [38]. It was attributed to good bonding between particles, enabling the deposit to behave like a monolithic material. Elastic modulus has also been characterized using micro- and/or nano-indentation, typically by comparing indentations between a surface sectioned in the plane of the deposit and a surface sectioned through the thickness [31,32,39]. One study found the modulus to be isotropic [39], attributed to the same cause as in the RUS study. Another study found modulus to be anisotropic, with a higher value in the through-thickness cross-sections than in the in-plane sections [31]. This was attributed to a greater amount of cold working across the through-thickness section. Hardness has also been characterized using nano- and/or micro-indentation [31,32,34,39]. The same study that found elastic modulus to be isotropic also found hardness to be isotropic [39], attributed to the same cause. Most of the studies, however, measured higher hardness in the through-thickness versus the in-plane section, for either the same reason that elastic modulus was higher in this section [31], or because a higher proportion of fine-grained particle interfaces are present in this section [32]. Several groups have characterized the tensile properties (tensile strength and/or elongation at break) in cold spray deposits [31,32,34,40]. Most of these groups performed tests on specimens machined from the two in-plane directions: the long-rastering and stepping directions [31,32,34,40]. One group found isotropy between these two directions [40], but the others found the properties to be lower in the stepping direction, due to a lower bond strength between adjacent tracks as opposed to along the direction of the tracks [31,32]. One study also characterized the tensile properties in the through-thickness direction [32] and found them to differ from the values measured in the in-plane directions, due to the differing modes of fracture between particles when loaded in the through-thickness direction (opening mode) versus the in-plane directions (shear mode). Although these studies have made significant strides in revealing the extent and causes of anisotropy in cold spray deposits, the authors of the present study know of no studies, to date, that have focused on the anisotropy of critical fracture toughness.

The goal of the present study is two-fold: (i) to investigate the fundamental nature of critical fracture in cold spray deposits for different crack orientations, and (ii) to quantify the level of anisotropy in critical fracture toughness. To this end, the fracture strength of as-sprayed bulk Al 6061 cold spray deposits is characterized using the ASTM E399 compact tension test. Six different crack orientations, relative to the spray directions, are tested, and the results are compared between them. The results are also compared to those from tests conducted on wrought Al 6061-T6 alloy. Finally, the anisotropy in fracture toughness is related to microstructural and fractographic features of the deposits, via light and scanning electron microscopy.

2. Materials and methods

2.1. Feedstock powder and substrate

In this study, Al 6061 was chosen as the feedstock powder because of its common use in cold spray applications, its ready availability, and the fact that its tensile mechanical properties have been studied extensively in the cold spray literature. The latter allows a basis for comparison for the present findings. Military specification (Mil-DTL-32495C, Amendment 2 [168]) powder was acquired from Valimet® (Stockton, CA, USA). Pre-spray particle size distribution was characterized using light microscopy and image analysis (c.f. Table 1). Per the manufacturer's recommendation for removing adsorbed moisture from the powder prior to spraying, it was heat treated in air at 230 °C for one hour, then allowed to cool to room temperature. It was subsequently stored in a dry nitrogen glovebox until spraying.

Substrate material consisted of 6.35-mm (1/4-in.) thick Al 6061-T651 plate stock. Surface preparation was performed by hand abrading with 3 M® Scotch-Brite pad, followed by cleaning with 100% ethanol. Spraying was subsequently conducted using the spray parameters listed in Table 1. To ensure consistency between each spray, particle velocity measurements were taken at the end of each, using an Oseir® HiWatch HR (Tampere, Finland) laser particle tracking velocimetry system.

Table 1
Spray parameters.

| Spraying System | VRC® Gen III Max |
|--------------------------|--|
| Powder Type | Valimet® Al 6061, Mil-DTL-32495C, Amend. 2, 230-mesh |
| Powder Size Dist. | 19 µm (D10), 34 µm (D50), 51 µm (D90) |
| Substrate | Al 6061-T651, 6.35-mm (1/4-in.) Plate |
| Powder Feed Rate | 6.1 g/min |
| Gas Type | Helium |
| Gas Pressure | 3.5 MPa |
| Gas Temperature | 400 °C |
| Nozzle Material | polybenzimidazole (PBI) |
| Nozzle Model | VRC® Nozzle 0071 |
| Nozzle Throat Length | 2.7 mm |
| Nozzle Length | 170 mm |
| Nozzle Throat Diameter | 1.75 mm |
| Nozzle Exit Diameter | 4.85 mm |
| Nozzle Standoff Distance | 25.4 mm |
| Rastering Speed | 254 mm/s |
| Rastering Step Size | 1 mm |
| Particle Velocity | 1110 ± 160 m/s |

2.2. Direction conventions

The notation prescribed in ASTM E8 [41] for defining the directions in wrought plate stock is adapted to the cold spray deposits in the present study. The long rastering direction is defined as the longitudinal, L, direction, the stepping direction as the transverse, T, direction, and the through-thickness direction as the short transverse, S, direction (Fig. 1). For defining crack orientation in the fracture samples, the paired-script convention in ASTM E399 is adopted, the first script corresponding to the direction of applied load, and the second script corresponding to direction of crack propagation (Fig. 1). For example, the T-S orientation corresponds to that in which the load is applied in the T direction and the crack propagates in the S direction. Using this convention, six fundamental crack orientations can be specified, as shown in Fig. 1.

2.3. Porosity measurements

Porosity measurements were made using the area percentage method specified in ASTM E2109-01 [42] using a sample from each of the three principle planes in the deposit—the S-T/T-S plane, the S-L/L-S plane, and L-T/T-L plane. Metallographic preparation was performed according to ASTM E3 [43], and light microscopy was performed on a Zeiss Axioscope® 7 MAT (Carl Zeiss AG, Oberkochen, Germany). Three images were taken on each deposit plane, and porosity was measured using contrast-based image analysis.

2.4. Fracture tests

In the present study, two slightly different sizes of the ASTM E399 [27] compact tension specimen were used (Fig. 2). The specimen size depicted in Fig. 2a was based upon a characteristic length, W of 25 mm (as specified in the standard), and it was used to fabricate the L-T and T-L fracture specimens. The specimen size in Fig. 2b is a 4:5-scale version of the 25-mm specimen, with a characteristic length of 20 mm. It was used to fabricate the S-T, T-S, S-L, and L-S specimens. This scaling was done to accommodate a maximum deposit height limit as a result of a limited supply of helium, per spray. Such scaling is allowed by ASTM E399 and has no nominal effect on fracture toughness, so long as the test methodology and validity criteria in the standard are properly followed and met.

Deposits were sprayed to accommodate between two and four fracture specimens from each crack orientation. Velocimetry measurements at the end of each were consistent, indicating that no major changes in spray parameters occurred during spraying. An overall range of 1110 ± 160 m/s was measured, as indicated in Table 1. Following spraying, specimens were cut from each deposit using diamond saw sectioning, waterjet cutting, and surface end milling. All cutting processes used low cutting forces and liquid cooling to prevent mechanical and thermal damage to the deposit material.

Prior to testing, fatigue pre-cracking was performed on an Instron® 1350 fatigue testing frame with a 100-kN load cell. Sinusoidal loading with a load ratio of $R = P_{min}/P_{max} = 0.1$ and a frequency of 50 Hz was used. Load shedding was employed to maintain an applied stress intensity factor between 0.6 and 0.8 K_{Ic} , until a sufficiently long pre-crack was developed (typically after 10^4 to 10^5 cycles). The fatigue crack growth rate during this process, da/dN , of $\sim 10^{-5}$ mm/cyc, was sufficiently low to produce a distinct morphological difference between the post-fracture fatigue and rapid crack propagation regions, such that the pre-crack was easily distinguishable. Following pre-cracking, fracture testing was performed on an Instron® 5582 universal testing apparatus with a 100-kN load cell at a crosshead displacement rate of 0.65 mm/min. A crack opening displacement (COD) gauge was used to measure the load line displacement during testing, and the 95% secant offset method was used to determine the critical load at fracture, in

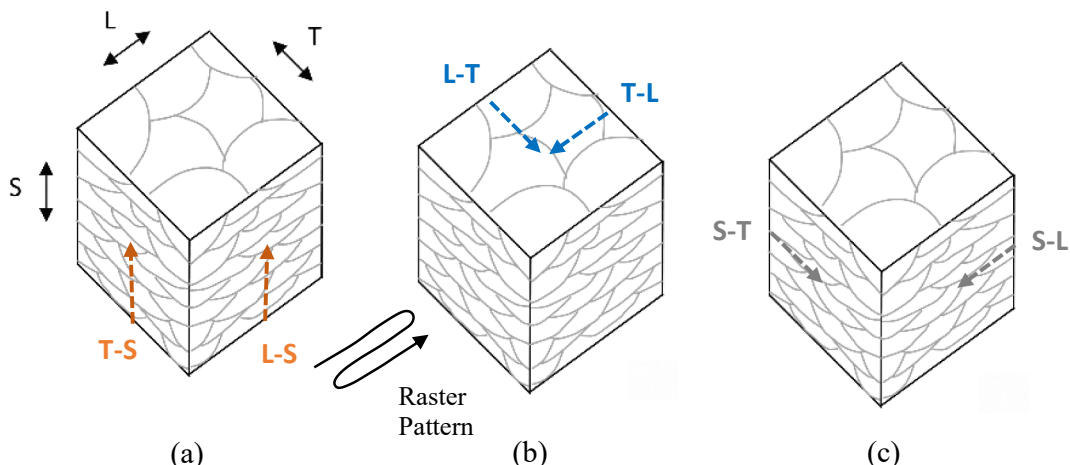


Fig. 1. The three fundamental directions and six basic crack orientations available in a cold-spray deposit: L the long rastering (“longitudinal”) direction, T the stepping (“transverse”) direction, and S the through-thickness (“short transverse”) direction. The dashed arrows indicate the crack propagation directions. For each load/crack propagation direction pair (e.g. “L-T”), the first script corresponds to the direction of applied load, and the second script corresponds to direction of crack propagation, as defined in ASTM E399 [27].

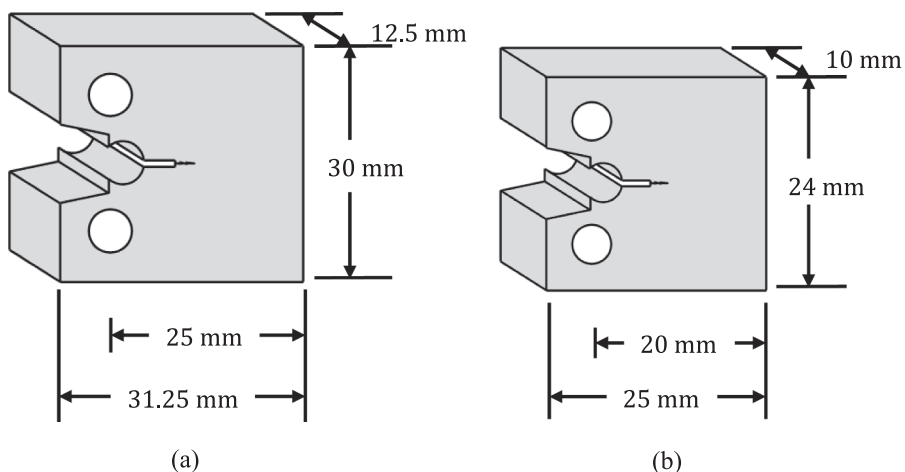


Fig. 2. The two compact tension specimen sizes used in the present study: (a) the 25-mm specimen used to fabricate the L-T and T-L specimens; (b) the 20-mm specimen used to fabricate the S-T, T-S, S-L, and L-S specimens.

accordance with ASTM E399 [27].

In addition to the cold-sprayed material, fracture tests were also performed on Al 6061-T6 wrought material. The wrought specimens were machined from 9.53-mm (3/8-in.) thick plate stock, then prepared and tested using the same procedures as the cold spray specimens. To avoid confusion with the L/T/S notation used for the cold spray specimens, the convention defined in ISO 12135 [44] is adopted, using X, Y, and Z to correspond to the rolling, in-plane transverse, and through-thickness directions, respectively. In the present study, while the mechanical properties were tested in all six directions for the cold spray deposits, only the in-plane (X-Y and Y-X) directions were tested in the wrought material. Most fracture values for wrought plate stock are only reported in these directions. Furthermore, the relative thinness of the wrought plate stock used in the present study precluded fabrication of specimens in the other four directions.

2.5. Residual stresses

Residual stresses in materials can have a significant effect on fracture toughness. For example, in a study on laser shock-processed Al 6061-T6 plate, Rubio-González, et al. [45] showed a 15% increase in fracture toughness when residual stresses up to -275 MPa were present. Thermal spray processes can produce high residual stresses in thick deposits. In cold spray deposits, while residual stresses up to or in excess of ± 100 MPa [46–48] are sometimes reported, residual stresses are often reported in the range of ± 50 MPa [47–51]. For Al 6061 sprayed using helium, Saleh, et al. [49] reported a range of ± 20 MPa, and Rokni, et al. [52] reported a range of ± 40 MPa. While not measured in the present study, the residual stresses in thick (4.5-mm) Al 6061 deposits were sprayed in a related study by the authors, using the exact same conditions as the present study (to be published in a separate paper). They were found to be in the range of ± 40 MPa. Since these residual stresses are small in comparison with those from studies such as Rubio-González, et al. [45], they were considered to have only a minor effect on the fracture and tensile properties and were not taken into account in the fracture analysis of the present study.

2.6. Tensile tests

Because the computation of fracture toughness in ASTM E399 requires values for elastic modulus, yield strength, and tensile strength, tensile tests were also performed on the deposit material. ASTM E8 [41] was used to determine the yield strength, tensile strength, and elongation to break, and ASTM E111 [53] was used to determine elastic modulus. The standard sub-size rectangular tension specimen from ASTM E8 was employed, with gage dimensions of $25 \times 6 \times 6$ mm ($L \times W \times T$). The tensile properties were measured in the two in-plane principal deposit directions, L and T, but due to the limitation on deposit height, specimens could not be machined in the S-direction. As allowed by ASTM E8, a 1% taper from the ends of the reduced parallel section to the center was included, in, to ensure that necking and fracture occurred within the gage region. Between four and six specimens were machined from the deposit material in each of the two principal directions. To provide a basis for comparison, specimens of both sizes were also machined from the wrought Al 6061-T651 plate stock, in the X and Y directions.

Testing was performed on an Instron® 5582 universal testing apparatus with a 100-kN load cell. A constant crosshead speed of 0.5 mm/min was used, and strain was measured using an extensometer with a 12.5-mm (0.5-in) gage length. Elastic modulus was first determined by loading and unloading the specimen in the elastic region for at least three cycles, then computing the mean elastic modulus, as specified by ASTM E111. Thereafter, the specimen was loaded up to the 0.2% offset yield point, at which point the strain gage was removed to prevent damage. A camera was subsequently used to record the gage extension to failure, which was used to compute the final elongation.

2.7. Fractography

Following fracture and tensile testing, fractography was performed on the fracture and tensile specimens, via light microscopy on metallographic cross-sections and scanning electron microscopy (SEM) on overhead views of the fracture surfaces. The cross-sectional specimens were ground and polished using the same procedure as the porosity specimens, then etched using Keller's etchant [54,55]. Light microscopy was performed on the same Zeiss Axioscope® 7 MAT as the porosity specimens, under a magnification range of $250\times$ to $1000\times$. The SEM microscopy was performed on a Thermo Scientific™ Scios DualBeam SEM over a magnification range of $250\times$ to $2000\times$, using an accelerating voltage of 5 kV and a beam current of 0.10 nA.

3. Results

3.1. Porosity measurements

The results of the porosity measurements indicated no statistically significant difference between the three deposit planes ($0.012 \pm 0.009\%$ for the S/T-T/S plane, $0.008 \pm 0.005\%$ for the S/L-L/S plane, and $0.012 \pm 0.005\%$ for the L/T-T/L plane). The overall mean of $0.011 \pm 0.006\%$ was very low, indicating a very dense deposit. While other studies on Al 6061 sprayed using helium have reported higher porosities ($1.3 \pm 0.4\%$ by Sabard and Hussain [37], 5% by Al-Hamdan, et al. [56]), this value is consistent with the porosity levels typically encountered in helium-sprayed Al 6061 in authors' cold spray facility.

3.2. Tensile tests

The tensile properties (elastic modulus, yield strength, tensile strength, and elongation at break) for both the wrought and cold-sprayed specimens are reported in Fig. 3.

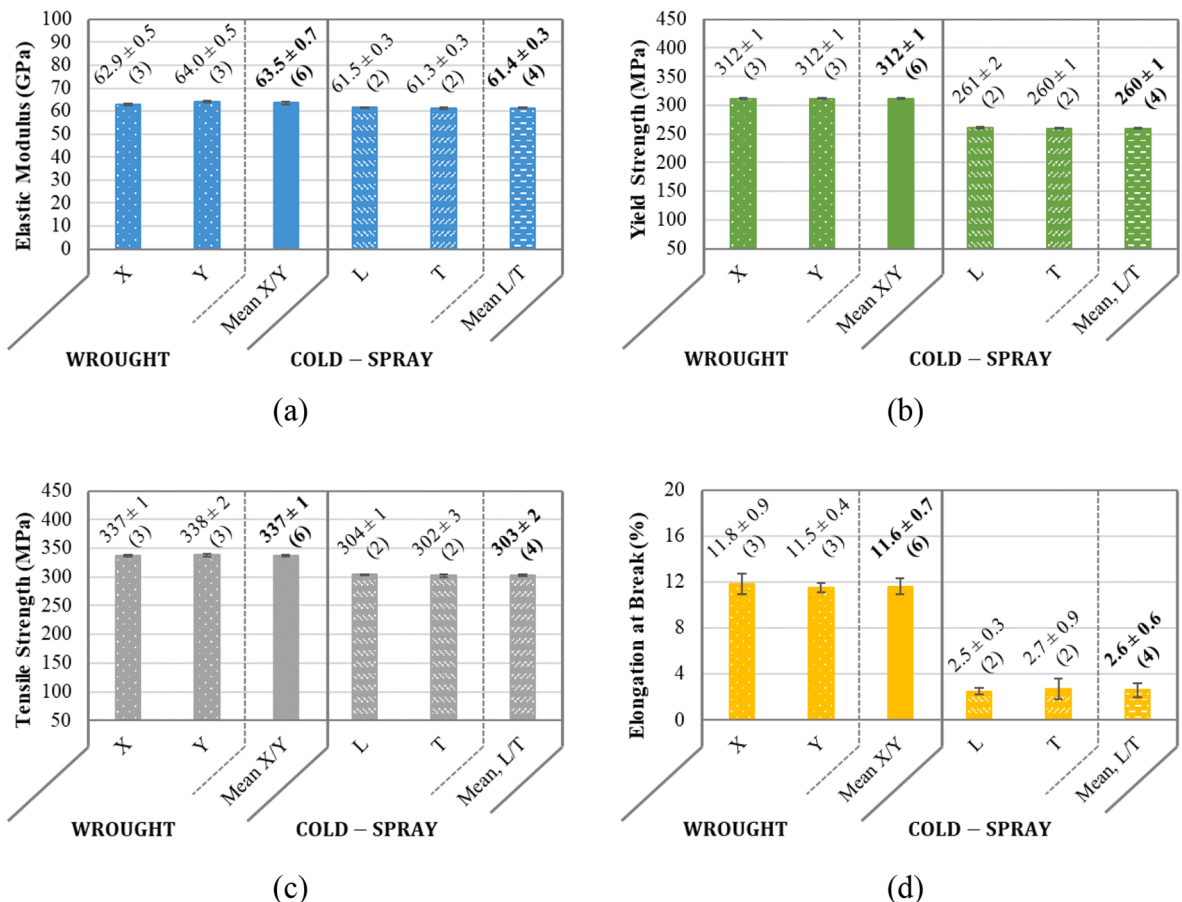


Fig. 3. Tensile properties from wrought and cold-sprayed Al 6061: (a) elastic modulus, (b) yield strength, (c) tensile strength, and (d) elongation at break. The mean and first standard deviation are given for each size/orientation combination, and the number of specimens tested for each is shown in parentheses.

3.3. Wrought material

The results of the tests on wrought Al 6061-T6 stock show that, aside from elastic modulus, there is no statistically significant difference in tensile properties between the X- and Y-directions. Consequently, yield strength, tensile strength, and elongation are expressed as overall means. While there is a slight difference for the elastic modulus results (62.9 ± 0.5 GPa for the X-direction versus 64.0 ± 0.5 GPa for the Y-direction), the difference is so minor that, for the purposes of this study, they have also been treated as statistically equivalent and expressed as an average value. A number of factors can affect elastic modulus, including grain size, grain orientation, residual stress, previous plastic strain history, and testing instrument precision [53], but, without further investigation – which is beyond the scope of this study – the exact reasons for the difference cannot be fully ascertained.

3.4. Cold spray material

Among the cold spray specimens, there is no significant anisotropy for all four mechanical properties between the L- and T- directions. The effect of a lower tensile strength and elongation in the T-direction due to lower bond strength between tracks – as reported by some [31,32,34] – appears not to be the case, here. This is probably partly due to the fact that the per-layer thickness in these studies (e.g. 1.625 mm/layer for Yin, et al. [32] and 1 mm/layer for Yang, et al. [31]) was an order of magnitude higher than in the present study (0.11–0.15 mm/layer), due to the use of much slower nozzle traverse speeds (20–50 mm/s) in these other studies versus in the present study (254 mm/s). Higher thickness per layer results in a much higher slope along the edges of tracks, resulting in a greater reduction in deposition efficiency along the edges of the tracks. In addition to this factor, the 1-mm step size used in the present study was significantly smaller than the 6-mm base width of the deposit, likely resulting in little morphological difference between the stepping and longitudinal directions. By contrast, while Yang, et al. [34] and Yang, et al. [31] do not state their step sizes, Yin, et al. [32] used a step size of 3.5 mm – almost half the average based width of a deposit track (5–7 mm, [2]).

In general, the above observations would suggest that anisotropy due to low inter-track bonding could be mitigated by depositing less material per track and using a smaller step size. However, while this may be acceptable in thin film applications such as wear-resistant coatings, it may be undesirable in additive manufacturing applications, where high deposition rates and low deposition times are often sought.

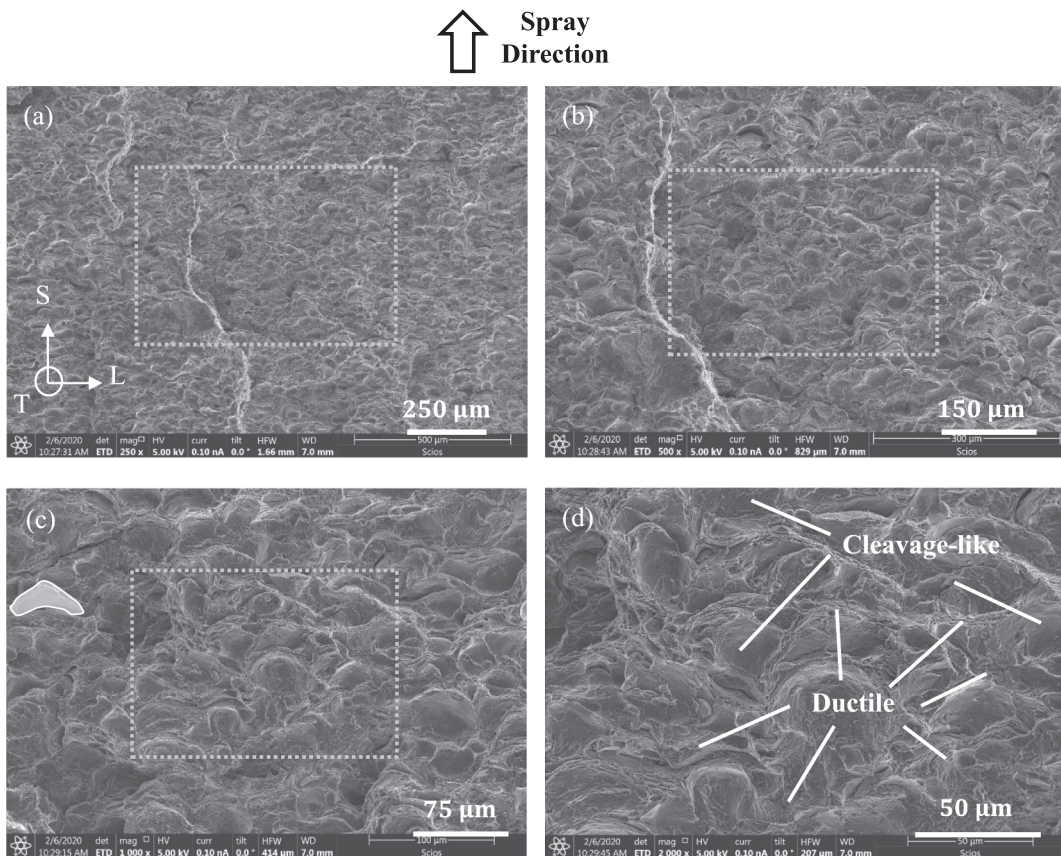


Fig. 4. SEM micrographs of the fracture surface of a T-oriented cold spray tensile specimen: (a) 250 \times magnification, (b) 500 \times , (c) 1,000 \times , (d) 2,000 \times . (Dashed boxes indicate the region from which the next magnification level was taken.)

For the cold spray specimens, the values for all four tensile properties were lower than those for the wrought specimens. The mean elastic modulus of the wrought standard-sized specimens was 63.5 ± 0.7 GPa, and the corresponding elastic modulus for the L/T cold sprayed (standard-sized) specimens was 61.4 ± 0.3 GPa, indicating a 3.3% decrease in modulus between wrought and cold sprayed material in the L/T orientation. For yield strength, tensile strength, and elongation, the cold sprayed specimens were 16–17% lower, 10–11% lower, and 77–78% lower than the wrought specimens, respectively. Gavras, et al. [5], using a similar set of spray parameters, observed similar drops in these properties for cold-sprayed Al 6061 versus wrought Al 6061-T6: a 4% decrease in elastic modulus, 10% decreases in yield strength and tensile strength, and an 88% decrease in elongation. They attributed the drop in elastic modulus to porosity and unbonded area between particles, which was hypothesized to be the same mechanism in the present study. Significantly reduced elongation is almost universally reported in the literature [4,5,23,52,57], and is attributed to the significant cold working of the particles and the limited metallurgical bonding between particles. Yield and tensile strength have been reported to either increase [52,57] or decrease [5], depending upon whether particle work hardening or limited interparticle bonding is dominant.

3.5. Fractography

Fig. 4 shows SEM micrographs of the fracture surface of a T-oriented cold spray tensile specimen. (Fracture surface images of the L-oriented specimens are morphologically similar and are omitted here.) At low magnification, (a) and (b), the surface shows the shapes of the particle boundaries, suggestive of a high degree of interparticular fracture (fracture along particle interfaces). At higher magnification, (d), a significant amount of cleavage-like fracture features are present, confirming this. Such morphology is common in tensile studies on as-sprayed cold spray deposits [6,7,52], most of which characterize their fracture as predominantly interparticular. However, at high magnification, there is also localized plastic microvoid coalescence. Some studies have characterized this as interparticular fracture at well-bonded particle interfaces [32], while others have characterized it as transparticular fracture (fracture through particles) [7]. In the present study, as will be explained further below, it is regarded as a combination of these two.

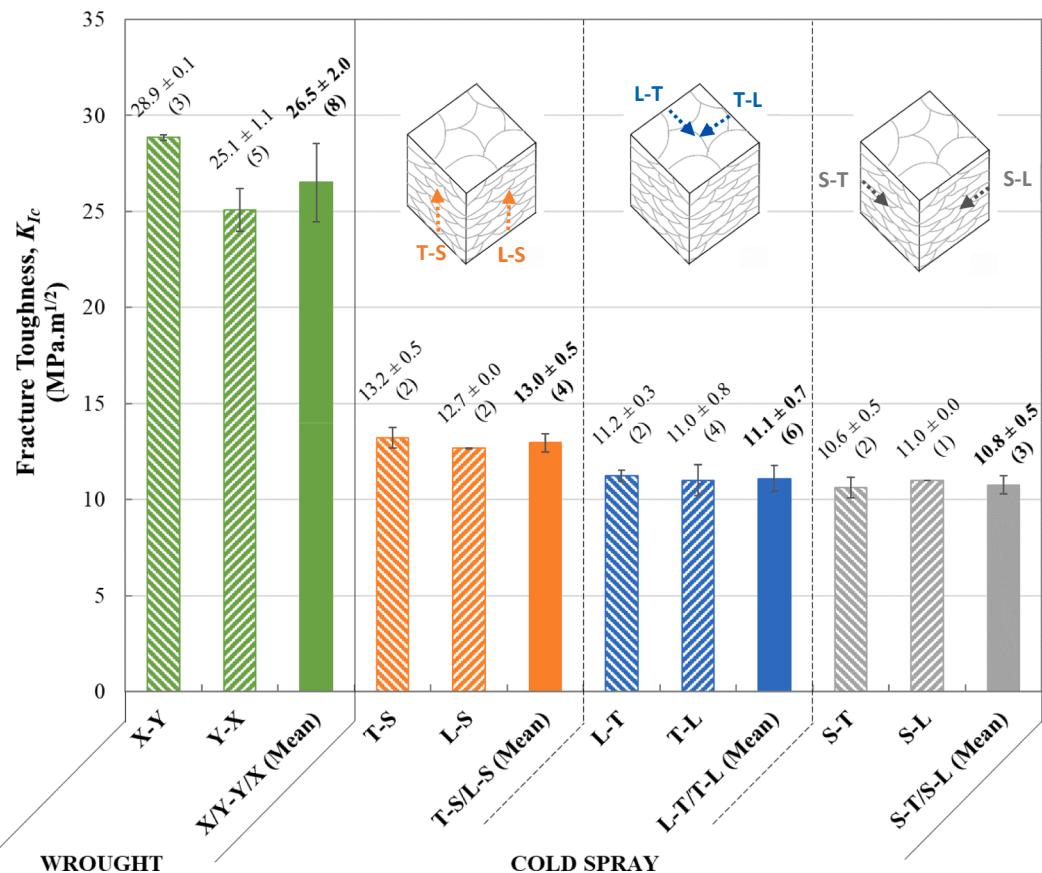


Fig. 5. Fracture toughness results of the wrought and cold spray specimens. Only the X-Y/Y-X orientations were tested for the wrought material – as is commonly done – due to insufficient thickness of the plate stock for machining upright specimens. All six crack orientations for the cold spray specimens (Fig. 1) were tested. Orientations are paired and color-coded according to similarity. For each orientation, the mean and first standard deviation are reported, along with the number of specimens tested in parentheses. (Note, for interpretation of the references to color in this figure, the reader is referred to the online version of this article.)

3.6. Fracture tests

[Fig. 5](#) summarizes the fracture toughness results for the wrought and cold spray material.

3.7. Wrought material

Prior to conducting fracture tests on cold spray material, the tests on wrought Al 6061-T6 were performed to ensure that there was no difference in results between the 20-mm and 25-mm specimen sizes and to validate the fracture testing method. Three specimens of the 20-mm size and five specimens of the 25-mm size were machined in the Y-X orientation. They were prepared and tested using the same procedure as for the cold sprayed specimens. The resulting mean fracture toughnesses were $24.9 \pm 0.6 \text{ MPa}\sqrt{\text{m}}$ for the 20-mm specimens and $25.1 \pm 1.1 \text{ MPa}\sqrt{\text{m}}$. As there was no statistically significant difference between these two values, it was concluded that the difference in specimen size had no bearing on the fracture toughness. Henceforth, only the results from the 25-mm samples are presented.

To validate the testing method, results were compared with literature reference values Al 6061-T6. ASM Handbook: Volume 19 [58] publishes a value of $29.1 \text{ MPa}\sqrt{\text{m}}$ for the Y-X orientation, obtained by using ASTM E399. This is 14% higher than the mean Y-X value in the present study. Another study, MacMaster, et al. [59], obtained a Y-X mean of $33.2 \pm 0.3 \text{ MPa}\sqrt{\text{m}}$ – 32% higher, but obtained using a different testing standard: ASTM E1820. While the difference in testing method may explain the discrepancy with the latter study, the discrepancy with the ASM-published value may simply be due to typical variation in mechanical property measurement between studies. The tensile properties in the present study measured by the standard-size specimens, for instance, were up to 20% different than the values published by ASM and in other literature studies [5,52,57]. Based on this, it was concluded that the wrought fracture values were sufficiently close to reference values to consider the testing method valid.

In [Fig. 5](#), there is a slight, statistically significant difference in mean toughness between the X-Y ($28.9 \pm 0.1 \text{ MPa}\sqrt{\text{m}}$) and Y-X ($25.1 \pm 1.1 \text{ MPa}\sqrt{\text{m}}$) orientations. This may be in keeping with the very slight difference in elastic modulus between the X and Y tensile directions ([Fig. 3](#)). Slight anisotropy is commonly present in wrought alloy stock, due to the metalforming process [60].

3.8. Cold spray material

The fracture results for the cold spray specimens are also shown in [Fig. 5](#). The tensile isotropy between the L and T (in-plane) directions would suggest that the six crack orientations can be paired as shown. For example, as a result of the in-plane tensile isotropy – as well as similar microstructural morphology between the two orientations – the T-S and L-S orientations would be expected to have similar fracture toughnesses. Indeed, this is the case, as there is no statistically significant anisotropy between them ($13.2 \pm 0.5 \text{ MPa}\sqrt{\text{m}}$ and $12.7 \pm 0.0 \text{ MPa}\sqrt{\text{m}}$, respectively). The same is true for the L-T and T-L orientations ($11.2 \pm 0.3 \text{ MPa}\sqrt{\text{m}}$ and $11.0 \pm 0.8 \text{ MPa}\sqrt{\text{m}}$, respectively) and S-T and S-L orientations ($10.6 \pm 0.5 \text{ MPa}\sqrt{\text{m}}$ and $11.0 \pm 0.0 \text{ MPa}\sqrt{\text{m}}$, respectively), where fracture toughnesses are each within error of one another, respectively.

With the above pairings, the mean fracture toughnesses of each pair are as follows: $11.1 \pm 0.7 \text{ MPa}\sqrt{\text{m}}$ for the L-T/T-L pair; $10.8 \pm 0.5 \text{ MPa}\sqrt{\text{m}}$ for the S-T/S-L pair; and $13.0 \pm 0.5 \text{ MPa}\sqrt{\text{m}}$ for the T-S/L-S pair. It is interesting to note the statistical isotropy between the L-T/T-L and S-T/S-L pairs. This was not expected, a priori. In the S-T/S-L pair, the crack plane was oriented parallel to the flattened plane of the particles, while, in the L-T/T-L pair, the crack plane was rolled 90° with respect to it. It was, therefore, expected that the S-T/S-L pair would have a lower fracture toughness. As will be described later, however, fractography revealed a similar fracture mechanism between the two pairs. The T-S/L-S pair exhibited a higher fracture toughness than the L-T/T-L and S-T/S-L pairs. This was expected, as the crack plane was oriented completely perpendicular to the flattened plane of the particles.

The above results can be summarized as follows: when the direction of the crack path was in the plane of the deposit (i.e. the L-T/T-L and S-T/S-L pairs), fracture toughness was equivalent (with an overall in-plane mean of $11.0 \pm 0.6 \text{ MPa}\sqrt{\text{m}}$). Crack plane orientation had no significant influence on toughness. When the direction of crack propagation was perpendicular to the plane of the deposit, fracture toughness was higher. Again, crack plane orientation had no significant influence. Overall, therefore, the deposit exhibited transversely isotropic fracture behavior.

In general, the cold spray fracture toughness results in [Fig. 5](#) span a range of approximately $11\text{--}13 \text{ MPa}\sqrt{\text{m}}$. This is approximately 40–50% of the fracture toughness of the wrought specimens and is similar to values from other studies on cold-sprayed aluminum alloys. Bakshi, et al. [8] obtained an L-S toughness value of $4.2 \text{ MPa}\sqrt{\text{m}}$ for helium-sprayed Al 1100; Bangstein, et al. [9] measured an L-T toughness of $3.0 \text{ MPa}\sqrt{\text{m}}$ for nitrogen-sprayed Al 6061; Gavras, et al. [5] obtained a maximum stress intensity factor of $10.2 \text{ MPa}\sqrt{\text{m}}$ in the L-T direction for helium-sprayed Al 6061; and Kovarik, et al. [11] obtained an L-S toughness for nitrogen-sprayed pure Al of $10.5 \text{ MPa}\sqrt{\text{m}}$.

3.9. Relationship between tensile and fracture properties

To serve as a check on the fracture toughness values, the Han and Rosenfield relationship between fracture toughness and tensile properties was employed to compute estimated fracture toughness values from the tensile properties measured in the present study. The equation is given by [61]

$$K_{Ic} \approx \sqrt{(2/3)E\sigma_{ys}\bar{\epsilon}^* n^2} \quad (1)$$

where E is the elastic modulus, σ_{YS} is the yield strength, $\bar{\epsilon}^*$ is the true strain to fracture, and n is the strain hardening exponent from Holloman's equation $\sigma_t = k\epsilon_t^n$. (Note that (1) is only valid where n is derived from experimental data where σ_t and k are in ksi units [61].) Equation (1) is capable of estimating the fracture toughness of titanium, steel, and aluminum alloys to within $\pm 30\%$ of experimentally-measured values. While the details can be found in Julien [62], the fracture toughness for the standard-sized wrought X- and Y-oriented specimens – computed using the mean X/Y tensile properties (Fig. 3) – was $22.6 \pm 0.7 \text{ MPa}\sqrt{\text{m}}$ – only 14.7% lower

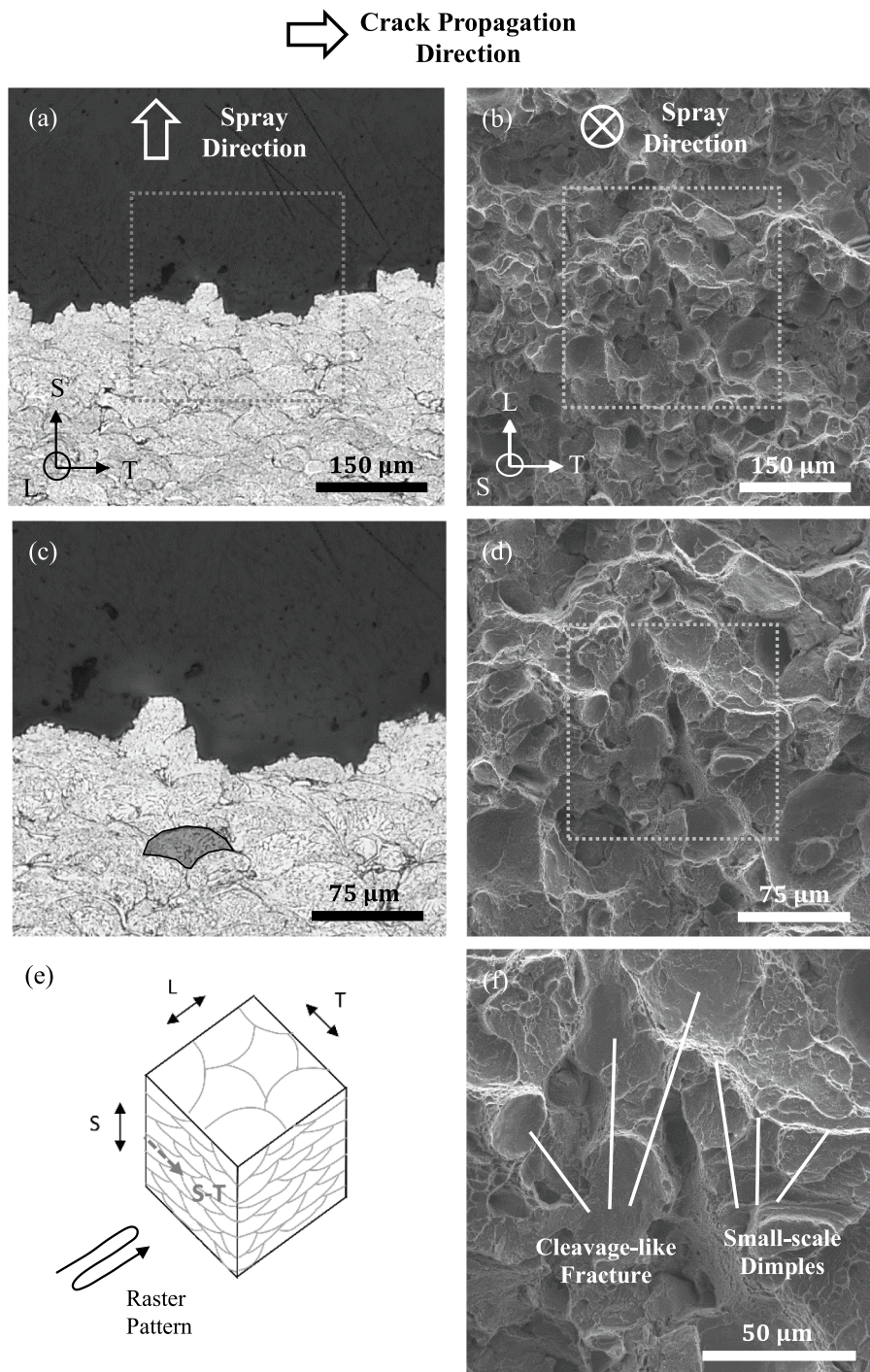


Fig. 6. Fracture surfaces of an S-T cold-spray fracture specimen: cross-sectional micrographs at (a) 500× and (c) 1,000×; SEM surface micrographs at (b) 500×, (d) 1,000×, and (f) 2,000×. Dashed boxes indicate the region from which the next magnification level was taken. To give perspective on characteristic size of particles, a single particle has been highlighted in (c). The load/crack configuration is shown in (e).

than the mean fracture toughness for wrought in the X-Y/Y-X orientations ($26.5 \pm 2.0 \text{ MPa}\sqrt{\text{m}}$; Fig. 5) and well within $\pm 30\%$ validity range for equation (1). For the cold spray specimens, the fracture toughness computed using the properties from the tensile tests (Fig. 3), was $9.6 \pm 1.1 \text{ MPa}\sqrt{\text{m}}$, only 12.7% lower than the mean in-plane fracture toughness of $11.0 \pm 0.6 \text{ MPa}\sqrt{\text{m}}$.

In addition to a quantitative verification, inspection of the H&R equation can shed some light into the reasons for the lower fracture toughness of the cold spray coatings. The value for n can be assumed to be approximately the same between wrought and cold spray

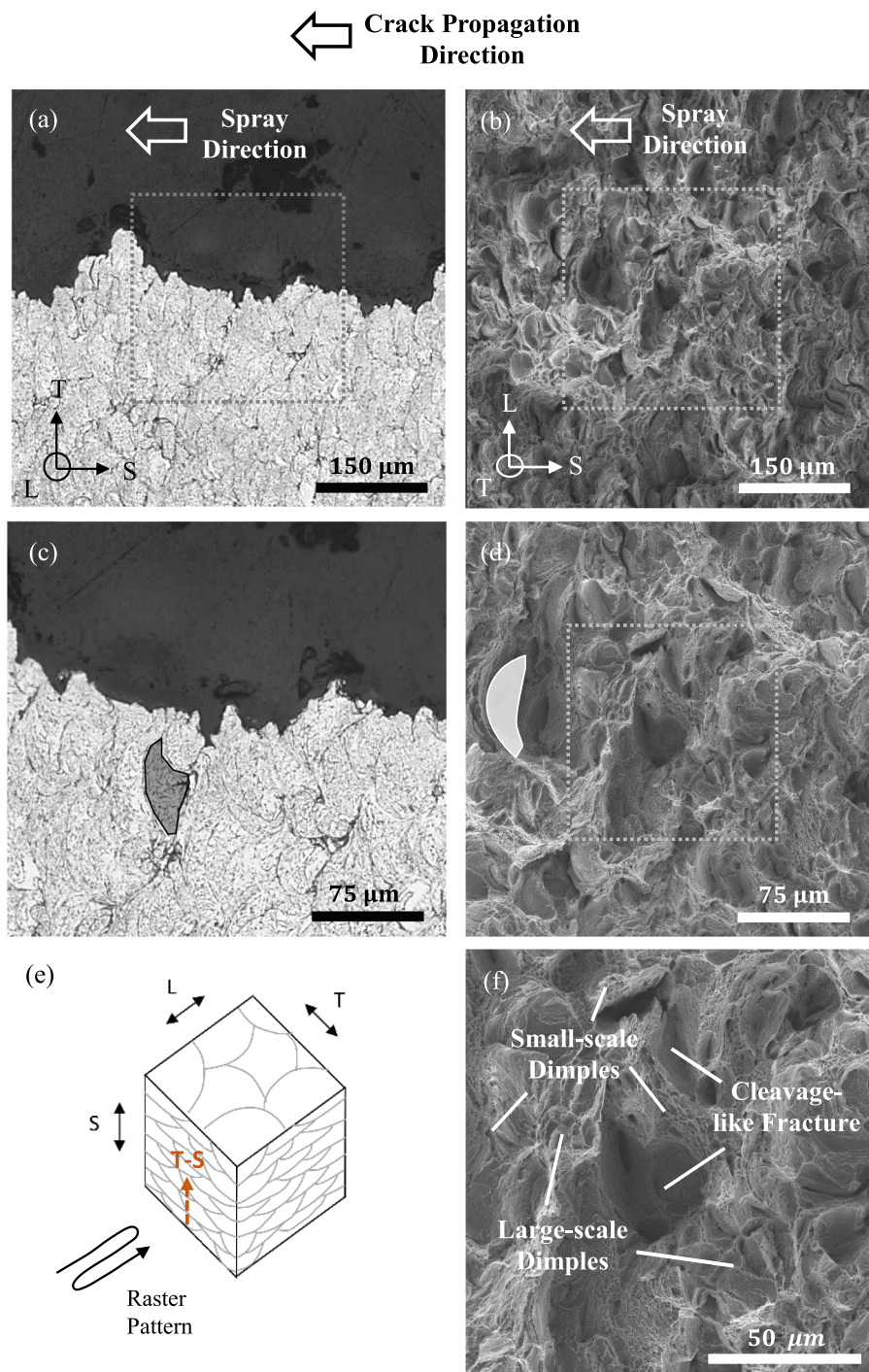


Fig. 7. Fracture surfaces of a T-S cold-spray fracture specimen: cross-sectional micrographs at (a) 500 \times and (c) 1,000 \times ; SEM surface micrographs at (b) 500 \times , (d) 1,000 \times , and (f) 2,000 \times . Dashed boxes indicate the region from which the next magnification level was taken. To give perspective on characteristic size of particles, a single particle has been highlighted in (c) and (d). The load/crack configuration is shown in (e).

specimens. The value for E is similar between the wrought and cold-sprayed specimens (only 3.3% lower for the latter), while the value for σ_{ys} is 16.7% lower for the cold spray specimens. The value for ϵ (and, correspondingly, $\bar{\epsilon}^*$), however, is significantly lower – 77.6% – suggesting that loss in ductility is the main contributor to the drop in fracture toughness in the cold spray deposits. Lower elongation has been attributed to decreased ductility of the particles as a result of cold working, as well as lower-than bulk inter-particle bond strength [52,63]. Increasing K_{Ic} has been achieved through optimized spray parameters that produce good as-sprayed particle bonding

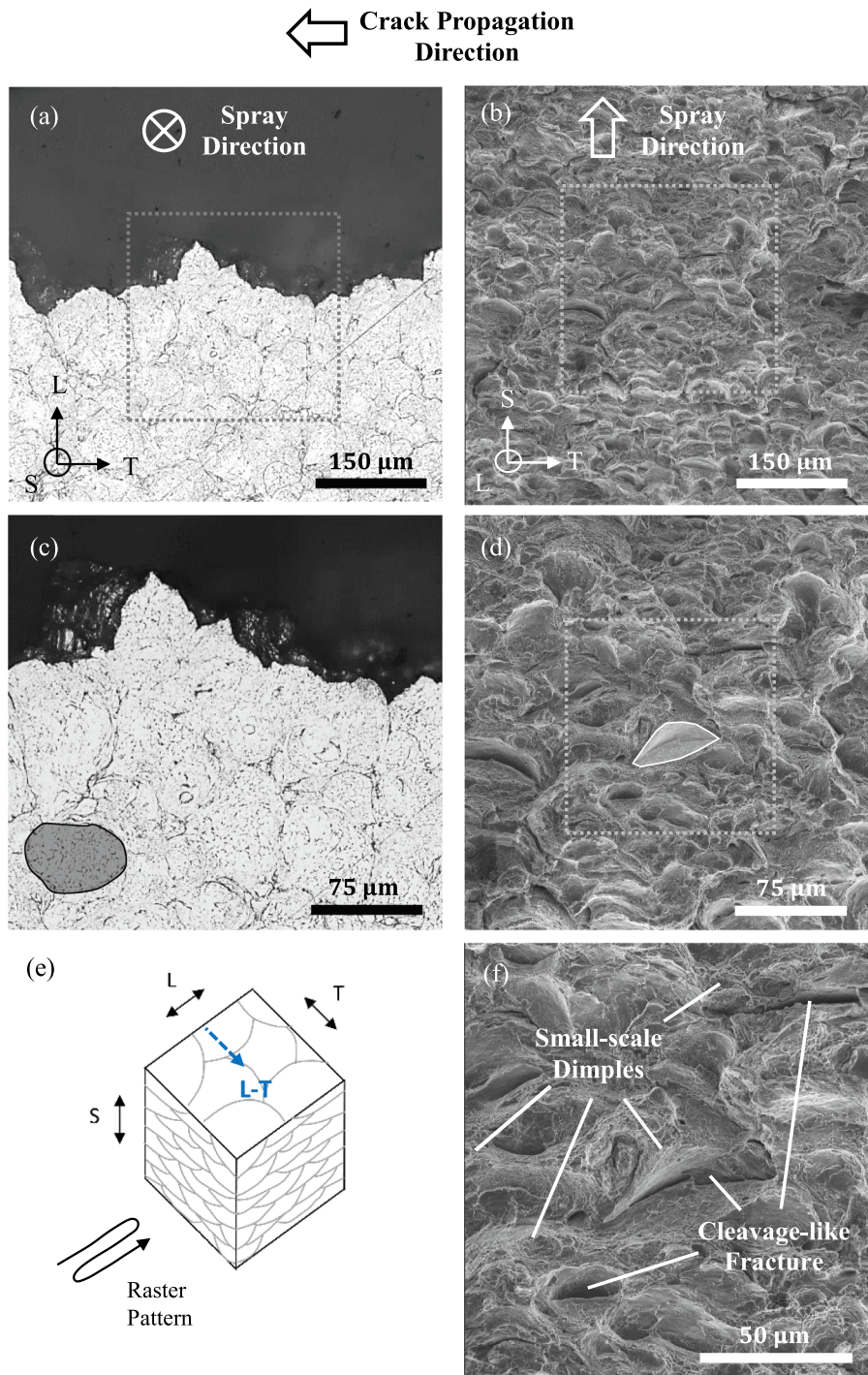


Fig. 8. Fracture surfaces of an L-T cold-spray fracture specimen: cross-sectional micrographs at (a) 500 \times and (c) 1,000 \times ; SEM surface micrographs at (b) 500 \times , (d) 1,000 \times , and (f) 2,000 \times . Dashed boxes indicate the region from which the next magnification level was taken. To give perspective on characteristic size of particles, a single particle has been highlighted in (c) and (d). The load/crack configuration is shown in (e).

[38,39], as well as post-spray heat treatments that improve particle bonding and recover the cold working in the particles [9,64].

3.10. Fractography

Fractographic images of representative fracture surfaces from each of the three load/crack orientation pairs are shown in Figs. 6 through 8. Fig. 6 shows cross-sectional light microscopy and surface SEM micrographs of the fracture surfaces from an S-T specimen, representative of the S-T/S-L crack orientation pair; Fig. 7 shows cross-sectional and surface micrographs of a T-S fracture specimen, representative of the T-S/L-S pair; and Fig. 8 shows cross-sectional and surface micrographs of an L-T fracture surface, representative of the L-T/T-L pair. Fracture surface images of corresponding S-L, L-S, and T-L surfaces are not given here because they are morphologically similar.

The fractography results of Figs. 6 through 8 shed some light as to the reason for the fact that higher toughness was observed when crack path direction was out-of-plane and equivalent toughnesses were observed when the crack path direction as in-plane. From the cross-sectional light microscopy images of the S-T specimen in Fig. 6, the crack path is tortuous, with the size of the peaks and crevices on the order of the particle size (as indicated by the outlined particle in (d)). This suggests interparticular fracture. In the SEM surface images, the surface is marked by the circular morphology of the flattened particles and a majority of cleavage-like fracture features, suggesting that interparticular fracture is the dominant mode. Some localized ductile plasticity is present, in the form of small-scale dimples, and these appear to be areas of interparticular fracture at well-bonded particle interfaces. This morphology resembles that of Gavras, et al. [5], who characterized their fracture as primarily interparticular and attributed the dimpling to interparticular metallurgical bonding at particle interfaces. This is not surprising, given that good metallurgical bonding has been experimentally observed at particle interfaces, elsewhere [35,65].

The morphology of the T-S specimen in Fig. 7 contrasts with that above. While the crack path in the light microscopy cross-sections is also tortuous, much of the tortuosity does not appear to follow the characteristic shape of particles in the fracture plane. Rather, it generally follows a smoother path, suggesting a high amount of transparticular fracture. In the SEM micrographs, there is a significant amount of dimpling present. Some of the dimples are on the same scale as those on the S-T surface in Fig. 6, suggesting some pullout of particles along well-bonded interfaces. Some of the dimples, however, are larger, suggesting fracture through a particle. Some features of cleavage-like fracture are also present on the surface, often in the form of crescent-shaped, smooth-walled cavities suggestive of out-of-plane particle pullout or in-plane opening of poorly-bonded particle interfaces. These features, however, are more sparse than in Fig. 6, suggesting that transparticular fracture played a major role, here. Bakshi, et al. [8] observed a similar fracture morphology in their L-S helium-sprayed Al 1100 fracture specimens, and they characterized their fracture as transparticular.

Finally, the fracture surface of the L-T specimen in Fig. 8 contains a mixture of both cleavage-like fracture and dimpling features that is intermediate to that of the S-T (Fig. 6) and T-S (Fig. 7) specimens. At first glance, this might suggest a mixture of interparticular and transparticular fracture that is intermediate between the two. However, the tortuosity of the fracture path on the fracture surface cross-section in Fig. 8 is on the order of the particle size. In addition, the dimples are small in scale, similar to those in Fig. 6; large-scale dimples characteristic of transparticular fracture (Fig. 7) are not present. Furthermore, many of the dimples are along the outer edges of the crescent-shaped smooth-walled cavities, suggesting shear failure along well-bonded regions of particle interfaces during particle pullout. These observations suggest that failure for the L-T/T-L specimens was largely interparticular like S-T/S-L specimens, but with perhaps a greater shear component than a normal one. Gavras, et al. [5] observed a similar fracture morphology in their fatigue fracture at near-critical stress intensity factors in L-T helium-sprayed Al 6061 specimens, and they similarly characterized their fracture as interparticular.

The difference in the amounts of transparticular and interparticular fracture between the different crack/load orientations may have a fracture mechanics explanation at the particle level. The propensity for a greater amount of transparticular fracture in the T-S/L-S orientations than in the S-T/S-L and L-T/T-L orientations may be due to the fact that the orientation of particle interfaces in the former (Fig. 9b and c) is almost entirely perpendicular to the global crack path (Fig. 9a). When fracture is transparticular (Fig. 9b), it possesses a high toughness, due to the high fracture energy associated with cohesive rupture of the particles. (The energy of bulk fracture through a particle – which can be estimated from the bulk fracture energy of wrought Al 6061 [66] – is on the order of 10^4 J/m^2 – much higher than the energy of interfacial fracture between particles. The latter is on the order of 1 to 10 J/m^2 and has been estimated from single particle impact experiments [67] and finite element simulations [68–70].) When fracture is interparticular, on the other hand (Fig. 9c), the fracture energy is lower, but the crack path is longer and fracture occurs predominantly in shear mode (mode II). The latter two factors increase the overall fracture toughness, possibly enough to make the interparticular fracture toughness equivalent to the transparticular toughness.

In contrast to the T-S/L-S orientations, interparticular fracture in the S-T/S-L and L-T/T-L orientations (Fig. 9d and e, respectively) exhibits a shorter crack path and a lower mode II component. For the S-T/S-L orientations (Fig. 9d), the fracture path is very straight, and the fracture mode is almost purely opening (mode I) – which has a lower toughness than mode II. For the L-T/T-L orientations, the crack is still moderately straight, and some mode I fracture is present in addition to mode II. These factors may result in an overall fracture toughness that is lower for interparticular fracture than transparticular.

The above line of reasoning may also explain why the global fracture toughness was higher in the T-S/L-S orientations than in the S-T/S-L and L-T/T-L orientations. The longer crack path and primarily mode II fracture of the former would have resulted in a higher overall fracture toughness. Furthermore, the equivalence in fracture toughness between the latter two orientations may be explained by the fact that the cohesive fracture energy of the particle is several orders of magnitude greater than interfacial fracture energy, while the fracture energies associated with mode I vs. mode II fracture are likely of the same order of magnitude (or only as much as one order of magnitude different). Since fracture in the S-T/S-L and L-T/T-L orientations contained little to no transparticular component, their

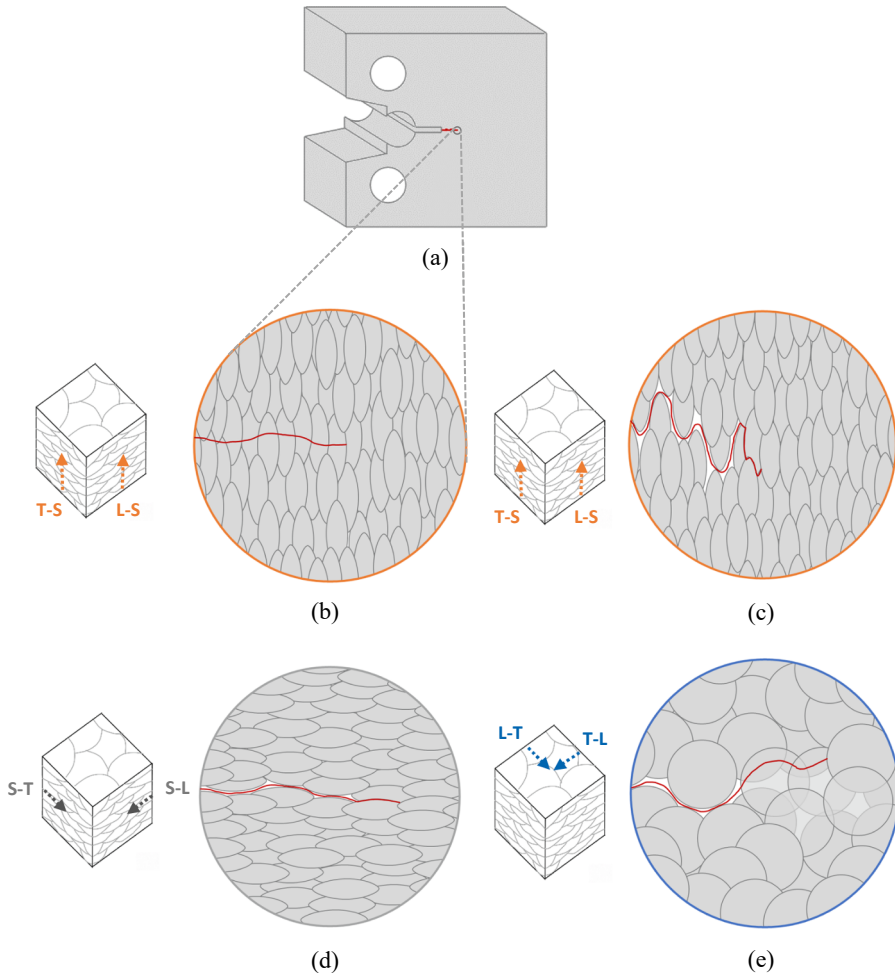


Fig. 9. Local crack path trajectories: (a) fracture specimen, (b) T-S/L-S configurations (transparticular), (c) T-S/L-S configurations (interparticular), (d) S-L/S-T configurations (interparticular), (e) L-T/T-L configurations (interparticular). Red lines indicate the crack path.

overall fracture toughnesses were, consequently, very close.

From the above discussion, it may be observed that three primary aspects of the fracture process at the particle level appear to influence the fracture toughness at the global level: the fracture energy (interfacial vs. bulk particle), the fracture mode (mode I vs. mode II), and the length of the fracture path. The interplay between these factors may determine whether transparticular or interparticular fracture is energetically favorable, as well as what the final global fracture toughness is. Additional investigation, however, is needed to further assess these hypotheses.

Overall, despite the presence of anisotropy in the present deposits, the difference in fracture toughness between the out-of-plane (T-S/L-S) and in-plane (S-T/S-L and L-T/T-L) orientations was only 15–20%. Given the significant microstructural difference between the out-of-plane and in-plane orientations as a result of the severely deformed particle morphology, this low level of anisotropy was somewhat surprising. However, the closeness of these values may be due to very good bonding between particles, as suggested by the qualitatively very compacted deposits, the very low porosity values, and the presence of appreciable plasticity in all of the fracture surfaces (Figs. 6, 7, and 8). Helium-sprayed Al 6061 generally has a high deposition efficiency and produces dense deposits [71], and the fact that the particle velocity (1110 ± 160 m/s) in the sprays in the present study was 1.7 times the critical velocity for Al on Al (approximately 650 m/s [72,73]) may have contributed to this.

4. Conclusions

In the present work, tensile and fracture anisotropy were studied in helium-sprayed bulk Al 6061 cold spray deposits. The findings can be summarized as follows:

4.1. Tensile properties

Tensile properties (elastic modulus, yield strength, tensile strength, and elongation at break) were measured in the two in-plane deposit (the long-rastering, L, and stepping, T) directions; the out-of-plane (S direction) was not tested.

- No anisotropy was observed for the properties, likely due to uniform in-plane microstructure as a result of small step size and high nozzle traverse speed.
- The tensile properties were lower than those for wrought, with values consistent with those from other studies.

4.2. Fracture toughness

Fracture toughness was characterized using the ASTM E399 compact tension specimen. Testing was performed in six principal load/crack direction pairs defined with respect to the spray directions.

- Fracture toughness was observed to be transversely isotropic. No anisotropy was observed when the crack path orientation was within the spray plane (in-plane, mean K_{Ic} of $11.0 \pm 0.6 \text{ MPa}\sqrt{\text{m}}$). Slightly higher fracture toughnesses were observed when the crack path orientation was perpendicular to the spray plane (out-of-plane, mean K_{Ic} of $13.0 \pm 0.5 \text{ MPa}\sqrt{\text{m}}$).
- The fracture toughness range was 40–50% that of wrought and consistent with other values in the literature.
- The in-plane fracture toughness values were consistent with the in-plane tensile properties, according to the classic Hahn and Rosenfield relation [61].
- In-plane fracture was characterized by almost 100% fracture between particles (interparticular), while out-of-plane contained a mixture of interparticular and transparticular fracture (fracture through particles).
- A greater amount of transparticular fracture was observed in orientations with higher fracture toughness.
- When fracture was primarily interparticular, local fracture mode (mode I or mode II) showed no significant influence on fracture toughness.
- Overall, anisotropy (15–20%) was low, likely due to good particle bonding as a result of the use of effective spray parameters and helium as the accelerating gas

Future studies would benefit from exploring the relationship between process parameters and fracture toughness. For example, the use of a different spraying gas (e.g. nitrogen instead of helium) may cause a greater or a lesser amount of anisotropy, depending upon the interplay between particle bond strength, degree of transparticular/interparticular fracture, etc. In addition, including measurement of other properties – such as microhardness, thermal conductivity, and/or electrical conductivity, for example – may further elucidate the nature and causes of the anisotropy in deposits. Finally, finite element or discrete element simulations of the fracture process at the particle level would help verify the suspected mechanisms underlying the propensity for transparticular versus interparticular fracture in the out-of-plane direction, including their relationship to the mechanical and interfacial properties of the particles.

CRediT authorship contribution statement

Scott E. Julien: Writing – review & editing, Writing – original draft, Methodology, Visualization, Software, Data curation, Formal analysis, Investigation. **Ahmad Nourian-Avval:** Validation, Investigation, Conceptualization. **Wentao Liang:** Data curation, Methodology, Validation. **Tricia Schwartz:** Validation, Resources, Investigation, Data curation. **Ozan C. Ozdemir:** Investigation, Methodology, Validation, Conceptualization, Data curation. **Sinan Müftü:** Writing – review & editing, Supervision, Project administration, Investigation, Funding acquisition, Conceptualization.

Declaration of Competing Interest

The authors declare that they have no known competing financial interests or personal relationships that could have appeared to influence the work reported in this paper.

Acknowledgements

Funding for this work was provided, in part, by: Raytheon Technologies; the United States (US) Army Research Laboratory (ARL), award no. W911NF-20-2-0024; the National Institute of Standards and Technology (NIST), award no. 70NANB21H007; the Eaton Corporation; and the US Army Corps of Engineers, Engineer Research and Development Center (ERDC), under OTA# W52P1J-20-9-3021; PPA CS-20-1201. In addition, the authors would like to thank the following individuals at Northeastern University for their contributions: Sam Boese and Jay Sanchez, for providing assistance and input on the sprays, and Jonathan Doughty and Benjamin MacAlister, for machining the tensile and fatigue test specimens and fixtures. The authors would also like to thank Robert Allegretto of VRC Metal Systems for providing assistance and technical guidance during the sprays.

References

- [1] Villafuerte J, editor. *Modern Cold Spray: Materials, Process, and Applications*. Springer; 2015.
- [2] Champagne VK, Ozdemir OC, Nardi A. Practical cold spray. Cham, Switzerland: Springer; 2021.
- [3] Villafuerte J. Current and future applications of cold spray technology. 2010/01/01/ Met Finish 2010;108(1):37–9. [https://doi.org/10.1016/S0026-0576\(10\)80005-4](https://doi.org/10.1016/S0026-0576(10)80005-4).
- [4] Champagne V, Nardi A, Cote D. Materials characterization of advanced cold-spray aluminum alloys. *Int J Powder Metall* 2015;51(4):37–47. Fall 2015.
- [5] Gavras AG, Lados DA, Champagne VK, Warren RJ. Effects of processing on microstructure evolution and fatigue crack growth mechanisms in cold-spray 6061 aluminum alloy. *Int J Fatigue* 2018;110:49–62.
- [6] Hall AC, Cook DJ, Neiser RA, Roemer TJ, Hirschfeld DA. The effect of a simple annealing heat treatment on the mechanical properties of cold-sprayed aluminum. *J Therm Spray Technol* 2006;15(2):233–8. <https://doi.org/10.1361/105996306x108138>. June 01.
- [7] Rokni MR, Widener CA, Champagne VK, Crawford GA, Nutt SR. The effects of heat treatment on 7075 Al cold spray deposits. *Surf Coat Technol* 2017;310:278–85.
- [8] Bakshi SR, Laha T, Balani K, Agarwal A, Karthikeyan J. Effect of carrier gas on mechanical properties and fracture behaviour of cold sprayed aluminium coatings. 2007/01/01 Surf Eng 2007;23(1):18–22. <https://doi.org/10.1179/174329407X161618>.
- [9] Bangstein B, Ellingsen M, Scholl N. A method of fracture toughness measurement and effect of partial annealing on monolithic thick cold sprayed aluminum 6061 deposits. In: ASME 2016 International Mechanical Engineering Congress and Exposition; 2016, pp. V002T02A082-V002T02A082.
- [10] White BC, Story WA, Brewer LN, Jordon JB. Fracture mechanics methods for evaluating the adhesion of cold spray deposits. *Eng Fract Mech* 2019;205:57–69.
- [11] Kovarik O, Siegl J, Cizek J, Charska T, Kondas J. Fracture Toughness of Cold Sprayed Pure Metals. 2020/01/01 J Therm Spray Technol 2020;29(1):147–57. <https://doi.org/10.1007/s11666-019-00956-z>.
- [12] Huang R, Fukanuma H. Study of the Influence of Particle Velocity on Adhesive Strength of Cold Spray Deposits. *J Therm Spray Technol* 2012;21(3):541–9. <https://doi.org/10.1007/s11666-011-9707-0>. June 01.
- [13] Li W-Y, Li C-J, Liao H. Significant influence of particle surface oxidation on deposition efficiency, interface microstructure and adhesive strength of cold-sprayed copper coatings. 2010/06/01/ Appl Surf Sci 2010;256(16):4953–8. <https://doi.org/10.1016/j.apsusc.2010.03.008>.
- [14] Mäkinen H, Lagerbom J, Vuoristo P. Adhesion of cold sprayed coatings: effect of powder, substrate, and heat treatment. Thermal Spray 2007: Global Coating Solutions 31–36 (2007).
- [15] Singh R, Schruefer S, Wilson S, Gibmeier J, Vassen R. Influence of coating thickness on residual stress and adhesion-strength of cold-sprayed Inconel 718 coatings. *Surf Coat Technol* 2018;350:64–73.
- [16] Xiong Y, Zhuang W, Zhang M. Effect of the thickness of cold sprayed aluminium alloy coating on the adhesive bond strength with an aluminium alloy substrate. *Surf Coat Technol* 2015;270:259–65.
- [17] ASTM C633. Standard Test Method for Adhesion or Cohesion Strength of Thermal Spray Coatings. West Conshohocken, PA: ASTM International; 2017.
- [18] Tan A-Y, Sun W, Bhowmik A, Lek JY, Marinescu I, Li F, et al. Effect of coating thickness on microstructure, mechanical properties and fracture behaviour of cold sprayed Ti6Al4V coatings on Ti6Al4V substrates. *Surf Coat Technol* 2018;349:303–17.
- [19] Yamauchi Y, Miyaji S. Interfacial state and characteristics of cold-sprayed copper coatings on aluminum substrate. IOP Conference Series: Materials Science and Engineering 61 012023 2014/08/01 (2014). 10.1088/1757-899x/61/1/012023.
- [20] Sova A, Grigoriev S, Okunkova A, Smurov I. Cold spray deposition of 316L stainless steel coatings on aluminium surface with following laser post-treatment. *Surf Coat Technol* 2013;235:283–9.
- [21] Schmidt T, Gaertner F, Kreye H. New developments in cold spray based on higher gas and particle temperatures. 2006/12/01 J Therm Spray Technol 2006;15(4):488–94. <https://doi.org/10.1361/105996306X147144>.
- [22] MIL-J-24445A. Military Specification, Joint, Bimetallic Bonded, Aluminum to Steel. Department of Defense; 1977.
- [23] Champagne VK, West MK, Reza Rokni M, Curtis T, Champagne V, McNally B. Joining of Cast ZE41A Mg to Wrought 6061 Al by the Cold Spray Process and Friction Stir Welding. *J Therm Spray Technol* 2016;25(1):143–59. <https://doi.org/10.1007/s11666-015-0301-8>. January 01.
- [24] Wang Q, Spencer K, Birbilis N, Zhang M-X. The influence of ceramic particles on bond strength of cold spray composite coatings on AZ91 alloy substrate. 2010/09/25/ Surf Coat Technol 2010;205(1):50–6. <https://doi.org/10.1016/j.surfcoat.2010.06.008>.
- [25] Sun W, Tan AWY, Marinescu I, Toh WQ, Liu E. Adhesion, tribological and corrosion properties of cold-sprayed CoCrMo and Ti6Al4V coatings on 6061-T651 Al alloy. *Surf Coat Technol* 2017;326:291–8.
- [26] Wang X, Feng F, Klecka MA, Mordasky MD, Garofano JK, El-Wardany T, et al. Characterization and modeling of the bonding process in cold spray additive manufacturing. *Addit Manuf* 2015;8:149–62.
- [27] ASTM E399. Standard Test Method for Linear-Elastic Plane-Strain Fracture Toughness KIc of Metallic Materials. West Conshohocken, PA: ASTM International; 2017.
- [28] ASTM E561. Standard Test Method for KR Curve Determination. West Conshohocken, PA: ASTM International; 2015.
- [29] ASTM E1820. Standard Test Method for Measurement of Fracture Toughness. West Conshohocken, PA: ASTM International; 2018.
- [30] ASTM E647. Standard Test Method for Measurement of Fatigue Crack Growth Rates. West Conshohocken, PA: ASTM International; 2015.
- [31] Yang K, Li W, Yang X, Xu Y. Anisotropic response of cold sprayed copper deposits. *Surf Coat Technol* 2018;335:219–27.
- [32] Yin S, Jenkins R, Yan X, Lupoi R. Microstructure and mechanical anisotropy of additively manufactured cold spray copper deposits. *Mater Sci Eng, A* 2018;734:67–76.
- [33] Lin E, Chen Q, Ozdemir OC, Champagne VK, Müftü S. Effects of interface bonding on the residual stresses in cold-sprayed Al-6061: A numerical investigation. 2019/02/01 J Therm Spray Technol 2019;28(3):472–83. <https://doi.org/10.1007/s11666-019-00827-7>.
- [34] Yang K, Li W, Guo X, Yang X, Xu Y. Characterizations and anisotropy of cold-spraying additive-manufactured copper bulk. 2018/09/01/ J Mater Sci Technol 2018;34(9):1570–9. <https://doi.org/10.1016/j.jmst.2018.01.002>.
- [35] Evans WC, Dan X, Houshamand A, Müftü S, Ando T. Microstructural characterization of aluminum 6061 splats cold spray deposited on aluminum 6061-T6 substrate. 2019/08/01 Metall Mater Trans A 2019;50(8):3937–48. <https://doi.org/10.1007/s11661-019-05303-z>.
- [36] Xiong Y, Bae G, Xiong X, Lee C. The effects of successive impacts and cold welds on the deposition onset of cold spray coatings. 2010/03/01 J Therm Spray Technol 2010;19(3):575–85. <https://doi.org/10.1007/s11666-009-9455-6>.
- [37] Sabard A, Hussain T. Inter-particle bonding in cold spray deposition of a gas-atomised and a solution heat-treated Al 6061 powder. 2019/09/01 J Mater Sci 2019;54(18):12061–78. <https://doi.org/10.1007/s10853-019-03736-w>.
- [38] Seiner H, Cizek J, Sedlák P, Huang R, Cupera J, Dlouhy I, et al. Elastic moduli and elastic anisotropy of cold sprayed metallic coatings. *Surf Coat Technol* 2016;291:342–7.
- [39] Bolelli G, Bonferroni B, Koivuluoto H, Lusvarghi L, Vuoristo P. Depth-sensing indentation for assessing the mechanical properties of cold-sprayed Ta. 2010/12/25/ Surf Coat Technol 2010;205(7):2209–17. <https://doi.org/10.1007/j.surfcoat.2010.08.146>.
- [40] Coddet P, Verdy C, Coddet C, Debray F. Mechanical properties of Cu-0.1Ag alloys deposited by cold spray with various powder feed rate and heat treatment. 2015/01/01 J Therm Spray Technol 2015;24(1):119–25. <https://doi.org/10.1007/s11666-014-0159-1>.
- [41] ASTM E8. Standard Test Methods for Tension Testing of Metallic Materials. West Conshohocken, PA: ASTM International; 2016.
- [42] ASTM E2109-01. Standard Test Methods for Determining Area Percentage Porosity in Thermal Sprayed Coatings. West Conshohocken, PA: ASTM International; 2014.
- [43] ASTM E3. Standard Guide for Preparation of Metallographic Specimens. West Conshohocken, PA: ASTM International; 2017.
- [44] ISO 12135. Unified Method of Test for the Determination of Quasistatic Fracture Toughness. Geneva, Switzerland: International Organization for Standardization; 2016.

- [45] Rubio-González C, Ocaña JL, Gomez-Rosas G, Molpeceres C, Paredes M, Bandera A, et al. Effect of laser shock processing on fatigue crack growth and fracture toughness of 6061-T6 aluminum alloy. *Mater Sci Eng, A* 2004;386(1-2):291–5. <https://doi.org/10.1016/j.msea.2004.07.025>.
- [46] McCune RC, Donlon WT, Popoola OO, Cartwright EL. Characterization of copper layers produced by cold gas-dynamic spraying. 2000/03/01 *J Therm Spray Technol* 2000;9(1):73–82. <https://doi.org/10.1361/105996300770350087>.
- [47] Luzin V, Spencer K, Zhang MX. Residual stress and thermo-mechanical properties of cold spray metal coatings. 2011/02/01/ *Acta Mater* 2011;59(3):1259–70. <https://doi.org/10.1016/j.actamat.2010.10.058>.
- [48] Spencer K, Luzin V, Matthews N, Zhang MX. Residual stresses in cold spray Al coatings: The effect of alloying and of process parameters. 2012/05/25/ *Surf Coat Technol* 2012;206(19):4249–55. <https://doi.org/10.1016/j.surfcoat.2012.04.034>.
- [49] Saleh M, Luzin V, Spencer K. Analysis of the residual stress and bonding mechanism in the cold spray technique using experimental and numerical methods. *Surf Coat Technol* 2014;252:15–28.
- [50] Luzin V, Spencer K, Zhang M, Matthews N, Davis J, Saleh M. Residual stresses in cold spray coatings. In: Cavaliere P, editor. *Cold-Spray Coatings: Recent Trends and Future perspectives*. Cham: Springer International Publishing; 2018. p. 451–80.
- [51] Sinclair-Adamson R, Luzin V, Duguid A, Kannoopatti K, Murray R. Residual stress distributions in cold-sprayed copper 3D-printed parts. 2020/08/01 *J Therm Spray Technol* 2020;29(6):1525–37. <https://doi.org/10.1007/s11666-020-01040-7>.
- [52] Rokni MR, Widener CA, Ozdemir OC, Crawford GA. Microstructure and mechanical properties of cold sprayed 6061 Al in As-sprayed and heat treated condition. *Surf Coat Technol* 2017;309:641–50.
- [53] ASTM E111. Standard Test Method for Young's Modulus, Tangent Modulus, and Chord Modulus. West Conshohocken, PA: ASTM International; 2017.
- [54] Vander Voort GF. Metallography, principles and practice. ed. Materials Park, OH: Materials Park, OH : ASM International, 1999.
- [55] Handbook ASM. Volume 9, Metallography and Microstructures. Materials Park, Ohio: ASM International; 2004.
- [56] Al-Hamdan KS, Murray JW, Hussain T, Clare AT. Heat-treatment and mechanical properties of cold-sprayed high strength Al alloys from satellite feedstocks. *Surf Coat Technol* 2019;374:21–31.
- [57] Sharma M, Schreiber J, Eden T, Champagne V. Stress corrosion cracking resistance of cold-sprayed Al 6061 deposits using a newly developed test fixture. *Coatings* 2019;9(7):445. <https://doi.org/10.3390/coatings9070445>.
- [58] Handbook ASM. Volume 19, Fatigue and fracture. Materials Park, Ohio: ASM International; 1996.
- [59] MacMaster FJ, Chan KS, Bergsma SC, Kassner ME. Aluminum alloy 6069 part II: fracture toughness of 6061-T6 and 6069-T6. 2000/09/30 *Mater Sci Eng, A* 2000;289(1):54–9. [https://doi.org/10.1016/S0921-5093\(00\)00918-7](https://doi.org/10.1016/S0921-5093(00)00918-7).
- [60] ASM Handbook: Volume 8, *Mechanical testing and evaluation*. Materials Park, OH: Materials Park, OH: ASM International, 2000.
- [61] Hahn GT, Rosenfield AR. Sources of fracture toughness: the relation between K_{Ic} and the ordinary tensile properties of metals: applications related phenomena in titanium alloys. West Conshohocken, PA: ASTM International; 1968.
- [62] Julien S. Interface Adhesion and Fracture: From Nanoscale Metallic Islands to Cold-Spray Coatings. Northeastern University; 2020.
- [63] Rokni MR, Widener CA, Crawford GA, West MK. An investigation into microstructure and mechanical properties of cold sprayed 7075 Al deposition. *Mater Sci Eng, A* 2015;625:19–27.
- [64] Li W-Y, Li C-J, Liao H. Effect of annealing treatment on the microstructure and properties of cold-sprayed Cu coating. 2006/06/01 *J Therm Spray Technol* 2006;15(2):206–11. <https://doi.org/10.1361/105996306X108066>.
- [65] Brody HD, Dongare AM, Lee S-W, Aindow M. Engineered Materials and Materials Design of Engineered Materials (EMMDEM): Characterization of Cold-Sprayed Materials. University of Connecticut, Storrs, CT2021.
- [66] ASM Handbook Volume 2A. Aluminum Science and Technology. Materials Park, Ohio: ASM International; 2018.
- [67] Xie W, Alizadeh-Dehkarghani A, Chen Q, Champagne VK, Wang X, Nardi AT, et al. Dynamics and extreme plasticity of metallic microparticles in supersonic collisions. *Sci Rep* 2017;7(1):5073. <https://doi.org/10.1038/s41598-017-05104-7>.
- [68] Chen Q, Alizadeh A, Xie W, Wang X, Champagne V, Gouldstone A, et al. High-strain-rate material behavior and adiabatic material instability in impact of micron-scale Al-6061 particles. *J Therm Spray Technol* 2018;27(4):641–53. <https://doi.org/10.1007/s11666-018-0712-4>, April 01.
- [69] Yildirim B, Fukanuma H, Ando T, Gouldstone A, Müftü S. A numerical investigation into cold spray bonding processes. *J Tribol* 2014;137(1). <https://doi.org/10.1115/1.4028471>.
- [70] Yildirim B, Yang H, Gouldstone A, Müftü S. Rebound mechanics of micrometre-scale, spherical particles in high-velocity impacts. *Proc Royal Soc A: Math, Phys Eng Sci* 2017;473(2204):20160936. <https://doi.org/10.1098/rspa.2016.0936>.
- [71] Story WA, Brewer LN. Heat treatment of gas-atomized powders for cold spray deposition. 2018/02/01 *Metall Mater Trans A* 2018;49(2):446–9. <https://doi.org/10.1007/s11661-017-4428-8>.
- [72] Schmidt T, Gärtner F, Assadi H, Kreye H. Development of a generalized parameter window for cold spray deposition. 2006/02/01/ *Acta Mater* 2006;54(3):729–42. <https://doi.org/10.1016/j.actamat.2005.10.005>.
- [73] Champagne VK, Helfritch DJ, Dinavahi SPG, Leyman PF. Theoretical and experimental particle velocity in cold spray. *J Therm Spray Technol* 2011;20(3):425–31.